Basins of attraction in nonsmooth models of gear rattle

Joanna F. Mason * †, Petri T. Piiroinen ‡, R. Eddie Wilson †, and Martin E. Homer †.

March 14, 2008

Abstract

This paper is concerned with the computation of the basins of attraction of a simple one degree-of-freedom backlash oscillator using cell-to-cell mapping techniques. This analysis is motivated by the modelling of order vibration in geared systems. We consider both a piecewise linear stiffness model and a simpler infinite stiffness impacting limit. The basins reveal rich and delicate dynamics, and we analyse some of the transitions in the system's behaviour in terms of smooth and discontinuity-induced bifurcations. The stretching and folding of phase space are illustrated via computations of the grazing curve, and its pre-images, and manifold computations of basin boundaries using DsTool (Dynamical Systems Toolkit).

1 Introduction

Rattle is a potential problem in any geared system. In quiet operation, meshing gears are expected to be in permanent contact. However, gear teeth are typically manufactured with a clearance, known as the backlash, and consequently meshing teeth may repeatedly lose and re-establish contact and thus rattle. This behaviour is known as a backlash oscillation.

An idealised equation of motion for a symmetric 1:1 pair of meshing spur gears (see [Halse et al., 2007; Mason et al., 2007]) takes the form

$$\Phi'' + \delta\Phi' + 2\kappa B(\Phi) = 4\pi\delta - 4\pi^2\varepsilon\cos(2\pi t) - 2\pi\delta\varepsilon\sin(2\pi t), \tag{1}$$

where Φ denotes the relative rotational displacement of the gears, and δ and κ denote non-dimensionalised damping and stiffness coefficients respectively. Moreover ε describes the non-dimensional amplitude of an external forcing effect which acts *order one*, i.e., at a frequency equal to the gross rotation rate of the gears. As written here, the forcing models eccentric mounting of the gears, but similar formulations could be used to describe oscillation in the driving torque of the system. Here, that driving torque is held constant and is represented by the non-dimensional $4\pi\delta$ term on the right-hand side of the model. Furthermore, we suppose that the system is in quasi-steady operation, so that on average the constant drive torque balances the damping, and we consider only small oscillations about a constant running speed.

Model (1) is closed by prescribing the restoring torque between the gear pair, for which we use the nonsmooth *backlash function*

$$B(\Phi) = \begin{cases} \Phi - \beta, & \Phi \geq +\beta, \\ 0, & |\Phi| < \beta, \\ \Phi + \beta, & \Phi \leq -\beta, \end{cases} \tag{2}$$

*Corresponding author. Email address: joanna.mason@bristol.ac.uk,
†Bristol Centre for Applied Nonlinear Mathematics, University of Bristol, Bristol BS8 1TR, United Kingdom.
‡Department of Mathematical Physics, National University of Ireland, Galway, University Road, Galway, Ireland.

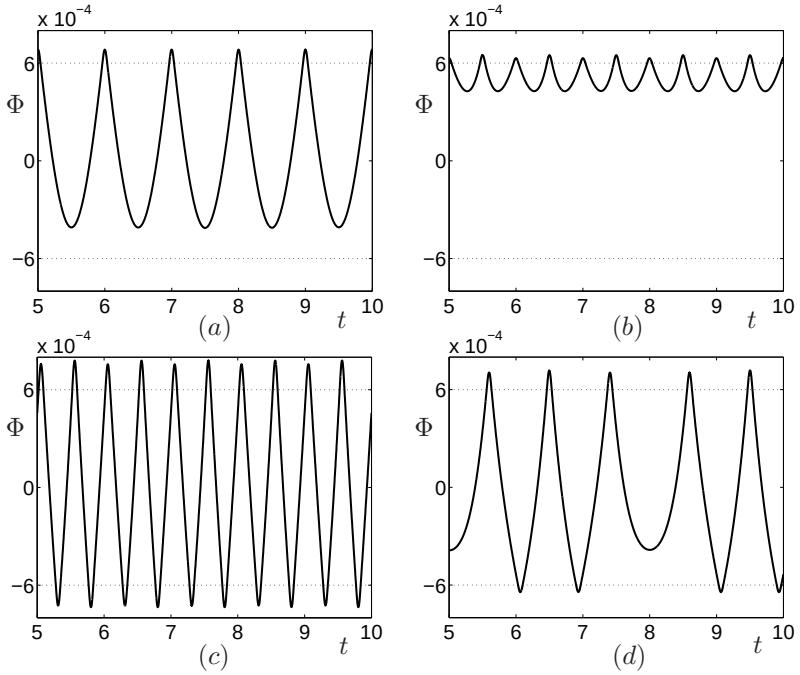

Figure 1: Some periodic solutions of Eqs. (1,2) for representative machine parameters $\kappa = 1000$, $\delta = 6 \times 10^{-4}$, $\beta = 6 \times 10^{-4}$ *and* $\varepsilon = 1 \times 10^{-4}$ *with the backlash boundaries* $\Phi = \pm\beta$ *overlaid in dotted lines. These solutions are linearly stable and coexist with a quiet solution (not shown) in which the gears are in permanent contact with* $\Phi \geq +\beta$. *Here note that the duration of contacts (for which* $\Phi \geq +\beta$ *or* $\Phi \leq -\beta$*) is extremely short, which motivates modelling the contacts by pure impacts.*

where 2β is the non-dimensional backlash width.

From the point of view of gear mechanics specialists, Eqs. (1,2) represent an over-simplified system, since we have neglected the parametric forcing effect (i.e., time-dependent stiffness) which operates at the tooth-meshing frequency (see for example [Theodossiades and Natsiavas, 2000; Blankenship and Kahraman, 1995]), by assuming that it is decoupled from the much slower order vibration operating at the gross rotation rate. Our interest is that Eqs. (1,2), which we call the *piecewise linear model*, constitute a piecewise smooth dynamical system (see [di Bernardo et al., 2007] for a review of this area) which has the potential for complex dynamics.

In fact, one may find a bound on the forcing term (see [Halse et al., 2007; Mason et al., 2007])

$$\varepsilon < \varepsilon_{\text{crit}}^{(1)} := \frac{2\delta}{\kappa}\sqrt{\frac{(\kappa - 2\pi^2)^2 + \pi^2\delta^2}{4\pi^2 + \delta^2}}, \tag{3}$$

which if satisfied, permits a 'quiet' solution for which $\Phi \geq +\beta$ for all time. This is simply the sinusoidal solution of a periodically forced linear oscillator, which we call the *permanent linear contact* (PLC) solution. However [Halse et al., 2007] found that even when Eq. (3) is satisfied, there may coexist families of periodic solutions that 'rattle', in the sense that $\Phi \geq +\beta$ does not hold for all time, see Fig. 1. Moreover, some of these rattling solutions are linearly stable and consequently real applications have the potential for intermittency or unreliability. The $t \to \infty$ dynamics depend upon the initial data, which in practice is difficult to control since it depends on fine details of the operating conditions and how a machine is run up from rest.

It is therefore a matter of practical concern to establish which linearly stable solutions dominate the $t \to \infty$ dynamics. Consequently, this paper is concerned with the computation of basins of

attraction for Eqs. (1,2) using cell-to-cell mapping techniques [Hsu and Guttalu, 1980; Hsu, 1987]. Moreover, our approach is motivated by an analysis of vibrations in the gearing mechanism of a Roots blower vacuum pump, which is a lightly damped system with very high stiffness. In this application, the rescaled damping δ, half backlash β and eccentricity ε are all small ($\sim 10^{-4}$), and the rescaled stiffness parameter κ is large ($\sim 10^{3}$). These parameters present a computational challenge for two independent reasons. Firstly, the large stiffness value introduces a small time-scale which must be resolved. Secondly, the small damping value gives rise to long transients and slender features in basin diagrams. This latter problem is severe for the parameter values quoted here, and consequently in this paper we work with scaled-up values for the purposes of illustration. However, we expect the qualitative details of the structures and transitions we observe to persist at more realistic parameter values.

As we observed in Fig. 1, in the large stiffness (large κ) limit, solutions tend to spend the majority of their time in the regime which we shall call *freeplay* (where $|\Phi| < \beta$), and in fact the duration of contacts scales like $1/\sqrt{\kappa}$. This motivates an *impacting contact* model [Halse et al., 2007] with coefficient of restitution one as a formal $\kappa \to \infty$ limit. As an alternative to Eqs. (1,2), we may thus analyse

$$\Phi'' + \delta\Phi' = 4\pi\delta - 4\pi^2\varepsilon\cos(2\pi t) - 2\pi\delta\varepsilon\sin(2\pi t), \qquad |\Phi| < \beta, \tag{4}$$

with perfectly elastic impact events at times $t_{\rm imp}$

$$\Phi'(t_{\rm imp}+) = -\Phi'(t_{\rm imp}-) \qquad \text{when} \qquad |\Phi(t_{\rm imp})| = \beta. \tag{5}$$

Here $\Phi'(t_{\rm imp}-) = \lim_{t\uparrow t_{\rm imp}} \Phi'(t)$ and $\Phi'(t_{\rm imp}+) = \lim_{t\downarrow t_{\rm imp}} \Phi'(t)$ are the velocities immediately before and after impact respectively. The perfect elasticity implies the absence of chattering (essentially, an infinite number of impacts in a finite time) which significantly simplifies our analysis and computations.

The impacting model is simpler to analyse than Eqs. (1,2) but has the disadvantage that it does not capture quiet solutions for which $\Phi \geq +\beta$ for all time. Consequently a proper understanding of the relative dominance of quiet and rattling behaviour can only be achieved by analysing Eqs. (4,5) in comparison with Eqs. (1,2). Other authors [de Souza and Caldas, 2001; de Souza et al., 2004, 2005] have computed basins of attraction for an impacting contact gear model and established the existence of chaotic regimes. But we go further and use Eqs. (1,2) to calculate the basins of attraction for quiet solutions — a matter of some importance from the engineering point of view.

Furthermore, we also describe more computationally-efficient methods by which the basins of attraction may be produced. In particular, we calculate stable manifolds, which form the basin boundaries, using Man1D, a module of DsTool [Back et al., 1992; Krauskopf and Osinga, 2000; England et al., 2004]. To our knowledge this is the first time that this package has been used to analyse a one degree-of-freedom backlash oscillator system such as the one described here

The outline of the paper is as follows. We begin by describing in detail the reduction of the impacting contact Eqs. (4,5) and full piecewise linear Eqs. (1,2) models to Poincaré maps, applied at the section $\Phi = +\beta$, in Secs. 2 and 3 respectively. These impact maps considerably simplify the analysis, visualisation and computations that follow. In particular, they enable the direct application of the *cell-to-cell mapping* technique, which we introduce in Sec. 4. Section 4 also describes our refinements to the cell-to-cell mapping technique, that we employ to minimise the effect of long transients. Basins of attraction for several ranges of parameter values (which all satisfy Eq. (3)) are computed in Sec. 5. We observe complicated dynamics and we present an explanation of some of the transitions in the system's behaviour in terms of smooth and discontinuity-induced bifurcations. In addition, in Sec. 6 we discuss the important role that the discontinuity in our system plays in the intricate stretching and folding of the phase space. Finally, in Sec. 7, we provide some concluding remarks and identify areas for further work.

2 Reduction to Map: Impacting Limit

The models Eqs. (1,2) and Eqs. (4,5) are non-autonomous single degree-of-freedom nonlinear oscillators with phase space (t, Φ, Φ'). In this paper we analyse their dynamics via their reduction to Poincaré maps. In such periodically forced systems, the usual approach is to reduce to a two-dimensional stroboscopic map which generates a sequence (Φ_0, Φ_0'), (Φ_1, Φ_1'), (Φ_2, Φ_2'), ..., at $t = 0, 1, 2, \ldots$. However, for our system it is more natural to use one of the impact conditions as the Poincaré section. This is because the impacting system Eqs. (4,5) is linear between impacts, and consequently we may exploit its explicit solution

$$\Phi(t) = c_1 + c_2 e^{-\delta t} + \varepsilon \cos 2\pi t + 4\pi t, \tag{6}$$

since this proves to be more efficient than solving the ordinary differential equation Eq. (4) by time integration. Note that a solution of Eqs. (4,5) consists of a sequence of segments described by Eq. (6) with the constants c_1 and c_2 repeatedly reset at impacts when $\Phi = \pm\beta$. Although Eq. (6) gives Φ explicitly in time, the task of finding times at which impact conditions $\Phi = \pm\beta$ apply reduces to the numerical solution of transcendental equations.

We now consider the itinerary of impacts. When $\Phi' = 0$, Eq. (4) yields

$$\Phi''(t) = 4\pi\delta - 2\pi\varepsilon(4\pi^2 + \delta^2)^{\frac{1}{2}} \cos(2\pi t + \xi), \tag{7}$$

where ξ is a phase shift. This expression is always positive provided

$$\varepsilon < \varepsilon_{\text{crit}}^{(2)} := \frac{2\delta}{(4\pi^2 + \delta^2)^{\frac{1}{2}}} \qquad (\sim \frac{\delta}{\pi} \quad \text{as} \quad \delta \to 0). \tag{8}$$

For sufficiently large κ, we have $\varepsilon_{\text{crit}}^{(1)} < \varepsilon_{\text{crit}}^{(2)}$, hence enforcing Eq. (3) guarantees the positivity of Φ'' at smooth local extrema. Hence local maxima of Φ are only possible at $\Phi = +\beta$ where Φ' is discontinuous, but local minima may be achieved smoothly for $|\Phi| < \beta$ or discontinuously at $\Phi = -\beta$, or (rarely) when $\Phi = -\beta$ and $\Phi' = 0$ simultaneously.

Let us now consider the fate of trajectories with initial data $-\beta < \Phi \leq +\beta$ and $\Phi' < 0$. Such a trajectory must impact at some subsequent time with either $\Phi = +\beta$ or $\Phi = -\beta$. To see this, assume the contrary, in which case Eq. (6) applies for all time, yielding $\Phi \to +\infty > +\beta$ as $t \to \infty$ and hence a contradiction. In the case where the next impact is with $\Phi = -\beta$, the velocity will reverse to a non-negative value. The subsequent impact after this one must be with $\Phi = +\beta$, since if the next impact were with $\Phi = -\beta$, a (smooth) local maximum would be required. Hence solutions must repeatedly return to the $\Phi = +\beta$ impact boundary, although they need not ever visit the $\Phi = -\beta$ boundary.

Thus $\Phi = +\beta$ defines a natural Poincaré section, and we work with a two-dimensional impact map P on $(t, v) \in [0, 1) \times (0, \infty)$ which describes times and velocities of impacts. Here time t is taken modulo one due to the period one forcing. By convention, we take $v = \Phi'(t-) = -\Phi'(t+) > 0$ for the velocity coordinate at impact at time t. Later, when the piecewise linear model Eqs. (1,2) is used, trajectories cross the surface $\Phi = +\beta$ and this idea needs refinement.

We now turn our attention to the structure of the impact map under consideration. To summarise our discussion above, there are two main outcomes (see Fig. 2) for a given initial condition with $\Phi = +\beta$ and $\Phi' = -v_0 < 0$ at time t_0:

Case (a) The next impact is with $\Phi = +\beta$, see Fig. 2(a).

Case (b) The next impact is with $\Phi = -\beta$ and the next but one impact is with $\Phi = +\beta$, see Fig. 2(b).

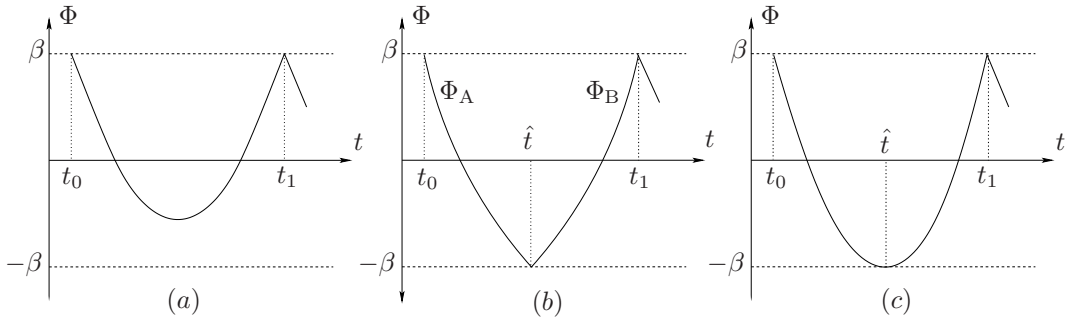

Figure 2: Sketches of the three different types of trajectory. From left to right : (a) illustrates a trajectory whose next impact is with the $\Phi = +\beta$ boundary, (b) a trajectory whose next impact is with the $\Phi = -\beta$ boundary before it re-impacts the $\Phi = +\beta$ boundary and (c) a grazing trajectory that grazes the $\Phi = -\beta$ boundary.

Furthermore, we have:

Case (c) The trajectory grazes the $\Phi = -\beta$ boundary with zero velocity before re-impacting the $\Phi = +\beta$ boundary, see Fig. 2(c).

In fact, case (c) separates cases (a) and (b) in the sense that if data (t_0, v_0^*) give rise to case (c), then (t_0, v_0) is case (a) if $v_0 < v_0^*$ or is case (b) if $v_0 > v_0^*$. This may be proven by a monotonicity argument which establishes that if Φ_1 and Φ_2 are solutions of Eq. (6) with initial data $\Phi_1(t_0) = \Phi_2(t_0) = \beta$ and $\Phi_1'(t_0) = -v_1$ and $\Phi_2'(t_0) = -v_2$ with $v_2 > v_1$, then $\Phi_1(t) > \Phi_2(t)$ for all $t > t_0$. The monotonicity principle itself may be established by noting that $\Phi_{\rm diff}(t) := \Phi_1(t) - \Phi_2(t)$ satisfies $\Phi_{\rm diff}'' + \delta\Phi_{\rm diff}' = 0$ from Eq. (4), together with $\Phi_{\rm diff}(t_0) = 0$, and so $\Phi_{\rm diff}(t) = A[1 - \exp(-\delta(t - t_0))]$.

For a given t_0, it follows that there is a unique $v_0^*(t_0)$ which satisfies case (c). Three example trajectories leaving the $\Phi = +\beta$ boundary at the same time with different initial velocities are illustrated in Fig. 3(a).

The remainder of this section describes how we construct the impact map on (t, v) pairs and how we tackle the resulting transcendental equations robustly. Section 2.1 sets up and solves systems of equations which define the grazing curve $v^*(t)$ described by case (c). Once this curve is computed, any given data (t, v) may be classified as case (a) (described in Sec. 2.2) or case (b) (described in Sec. 2.3). Note that the construction for case (b) poses particular difficulties since it consists of two trajectory segments, hence two impact times and two distinct root finding procedures.

2.1 Solution for the grazing curve

We begin by constructing trajectories that impact the $\Phi = -\beta$ boundary with zero velocity, see Fig. 2(c). Solutions of this type start at the $\Phi = +\beta$ boundary at time t_0 with velocity $\Phi'(t_0+) = -v_0^*(t_0)$ (to be determined) and graze the $\Phi = -\beta$ boundary at time $\hat{t}$ with zero velocity. Hence from Eq. 6 we have

$$(\Phi(t_0) =) \quad c_1 + c_2 e^{-\delta t_0} + \varepsilon \cos 2\pi t_0 + 4\pi t_0 = \beta, \tag{9}$$

$$(\Phi'(t_0) =) \quad -\delta c_2 e^{-\delta t_0} - 2\pi\varepsilon \sin 2\pi t_0 + 4\pi = -v_0^*, \tag{10}$$

$$(\Phi(\hat{t}) =) \quad c_1 + c_2 e^{-\delta \hat{t}} + \varepsilon \cos 2\pi \hat{t} + 4\pi \hat{t} = -\beta, \tag{11}$$

$$(\Phi'(\hat{t}) =) \quad -\delta c_2 e^{-\delta \hat{t}} - 2\pi\varepsilon \sin 2\pi \hat{t} + 4\pi = 0, \tag{12}$$

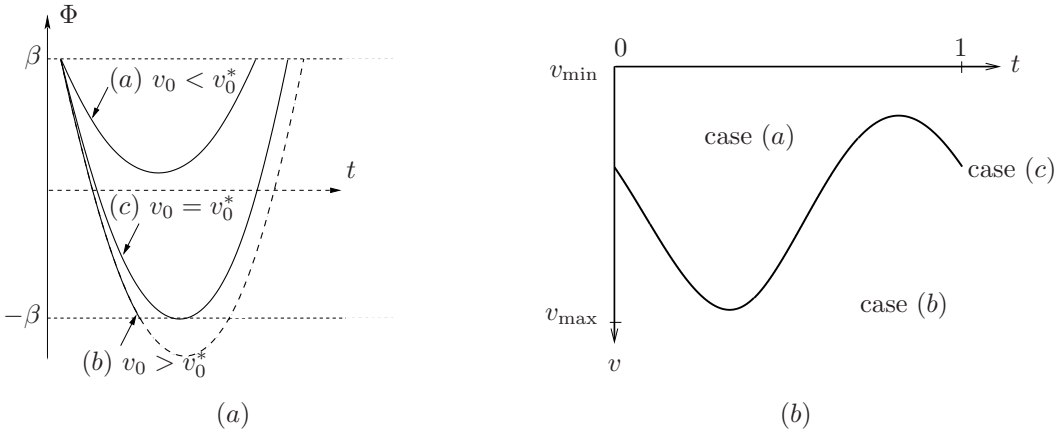

Figure 3: (a) Example trajectories of type (a), (b) and (c) leaving $\Phi = +\beta$ at the same time. Solid lines represent true trajectories, and the dashed lines, a trajectory ignoring the impact with $\Phi = -\beta$. (b) The division of (t, v) space into regions characterised by trajectories of type (a) and (b), by the grazing curve, (c).

as a system of four equations in the unknowns c_1, c_2, $\hat{t}$ and v_0^*. However, it is ultimately only v_0^* that is of interest.

If we subtract Eq. (11) from Eq. (9) and use Eq. (12) to substitute for c_2 we obtain a single equation

$$\frac{1}{\delta}(4\pi - 2\pi\varepsilon \sin 2\pi\hat{t})(e^{\delta(\hat{t}-t_0)} - 1) + \varepsilon(\cos 2\pi t_0 - \cos 2\pi\hat{t}) + 4\pi(t_0 - \hat{t}) - 2\beta = 0, \qquad (13)$$

to solve numerically for $\hat{t}$ as a function of t_0. The only remaining question concerns the counting of solutions and whether the solver finds the correct root. In this case provable robustness is not critical because the grazing curve $v^*(t)$ is computed in full prior to the basin computation, and a failure to find the correct root $\hat{t}$ for individual values of t_0 can be identified by visual inspection. However, in our examples no such problems occurred.

In fact, for each time t_0, it turns out that two values $\hat{t}$ satisfy Eq. (13), but only one of these satisfies $\hat{t} > t_0$. In the first instance we therefore solve Eq. (13) via the Newton method (see for example [Dahlquist and Björck, 1974]) with an initial guess $t_0 + 1/2$, and we have found that this converges to the correct root in all the cases that we have tried. Once $\hat{t}$ has been calculated for a single value of t_0, we compute further t_0, $\hat{t}$ pairs using a 'continuation' type method where t_0 is stepped in small increments and the solution $\hat{t}$ at one t_0-value is used as the Newton solver's initial guess for the next t_0-value. Each $\hat{t}$-value can then be converted to a corresponding velocity v_0^* using Eq. (10), and an interpolating curve $(t, v^*(t))$ is thus constructed. As we have discussed, this *grazing curve* acts as the separatrix of the trajectories whose next impact is with either the $\Phi = +\beta$ or $\Phi = -\beta$ boundary, see Fig. 3(b).

2.2 Case (a) : next impact with $\Phi = +\beta$

We now analyse trajectory segments of the form shown in Fig. 2(a), and thus we develop the impact map P for data $P(t_0, v_0) = (t_1, v_1)$ with $v_0 < v_0^*(t_0)$. We have

$$(\Phi(t_0) =) \quad c_1 + c_2 e^{-\delta t_0} + \varepsilon \cos 2\pi t_0 + 4\pi t_0 = \beta, \tag{14}$$

$$(\Phi'(t_0+) =) \quad -\delta c_2 e^{-\delta t_0} - 2\pi\varepsilon \sin 2\pi t_0 + 4\pi = -v_0, \tag{15}$$

$$(\Phi(t_1) =) \quad c_1 + c_2 e^{-\delta t_1} + \varepsilon \cos 2\pi t_1 + 4\pi t_1 = \beta, \tag{16}$$

$$(\Phi'(t_1-) =) \quad -\delta c_2 e^{-\delta t_1} - 2\pi\varepsilon \sin 2\pi t_1 + 4\pi = v_1, \tag{17}$$

cf. Eqs. (9-12). If we subtract (14) from (16), we solve $f(t_1) = \Phi(t_1) - \Phi(t_0) = 0$ for t_1 in terms of fixed t_0, which may be may be expanded using Eq. (15) to substitute for c_2, to give

$$f(t_1) = \frac{1}{\delta}\left(4\pi + v_0 - 2\pi\varepsilon \sin 2\pi t_0\right)\left(e^{-\delta(t_1 - t_0)} - 1\right) + \varepsilon(\cos 2\pi t_1 - \cos 2\pi t_0) + 4\pi(t_1 - t_0) = 0. \tag{18}$$

By using the relationship with Φ, we have $f(t_0) = 0$ and $f'(t_0) < 0$; moreover we have $\lim_{t\to\infty} f(t) = +\infty$. It follows that there is a unique root $t_1 > t_0$ which may be bracketed by successive doubling. Then either interval bisection or the method of false position will find the root robustly.

However, for δ small, a convexity argument may be used to establish the robust convergence of the Newton method. Note that $f(t)$ is not globally convex, even though it has a unique local minimum. To see this, we use Eq. (6) to derive

$$\Phi''(t) = \delta^2 c_2 \mathrm{e}^{-\delta t} - 4\pi^2 \varepsilon \cos 2\pi t, \tag{19}$$

which displays oscillatory behaviour as $t \to \infty$. However, since

$$c_2 = \frac{4\pi + v_0 - 2\pi\varepsilon \sin 2\pi t_0}{\delta} \mathrm{e}^{\delta t_0}, \tag{20}$$

a sufficient condition for convexity is given by

$$t < t_{\max} := t_0 + \frac{1}{\delta} \log_{\mathrm{e}} \left[\frac{\delta(4\pi + v_0 - 2\pi\varepsilon \sin 2\pi t_0)}{4\pi^2 \varepsilon} \right]. \tag{21}$$

Then $t_{\max} > t_0$ is established by showing that the argument of the logarithm exceeds one, for which it suffices that

$$\varepsilon < \varepsilon_{\mathrm{crit}}^{(3)} := \frac{\delta}{\pi + \delta/2} \sim \frac{\delta}{\pi}, \tag{22}$$

cf. Eq. (8), which thus generally holds throughout this paper. The interest however is in the limit $\delta \to 0$ with Eq. (22) maintained, for which $t_{\max} \to \infty$. In this case, successive doubling may be used to establish an interval which verifiably brackets the desired root t_1 and on which Φ and hence f are convex. The Newton method thus displays robust one-sided second order convergence for any initial guess in this interval which is to the right of the root.

2.3 Case (b) : next impact with $\Phi = -\beta$

We now proceed to construct trajectories that impact the $\Phi = -\beta$ boundary before re-impacting the $\Phi = +\beta$ boundary. Trajectories of this type consist of two pieces (see Fig. 2(b)), so two root finding procedures are required, to find the times of impact with the $\Phi = -\beta$ and $\Phi = +\beta$ boundaries respectively.

The first section of trajectory (Φ_{A}) starts from the $\Phi = +\beta$ boundary with initial times and velocities (t_0, v_0) and then impacts the $\Phi = -\beta$ boundary with unknown times and velocities $(\hat{t}, \hat{v})$. In addition to Eqs. (9) (replacing v_0^* by v_0), (10) and (11) we have

$$\Phi'(\hat{t}) = -\delta c_2 e^{-\delta \hat{t}} - 2\pi\varepsilon \sin 2\pi \hat{t} + 4\pi = \hat{v}. \tag{23}$$

If we subtract (9) from (11) and use (10) to substitute for c_2, we have

$$\frac{1}{\delta}\left(4\pi + v_0 - 2\pi\varepsilon\sin 2\pi t_0\right)\left(e^{-\delta(\hat{t}-t_0)} - 1\right) + \varepsilon(\cos 2\pi\hat{t} - \cos 2\pi t_0) + 4\pi(\hat{t} - t_0) + 2\beta = 0. \tag{24}$$

However (see Fig. 3(a)) this equation has two roots via its relationship to Φ and we seek only the left-most one for which a convexity argument applied to Φ may be used to establish the robust performance of the Newton method. To see this, note

$$\Phi'(t_{\max}) = 4\pi\left(1 - \frac{\pi\varepsilon}{\delta}\right) - 2\pi\varepsilon\sin 2\pi t_{\max}, \tag{25}$$

which is positive for ε sufficiently small and less than δ/π. Here $t_{\max}$ is given by Eq. (21). It follows that the local minimum of Φ is to the left of $t_{\max}$, and since $\hat{t}$ is to the left of the local minimum, Φ and hence f are convex on the interval $[t_0, \hat{t}]$. Hence for an underestimate of $\hat{t}$ such as $t_0 + 2\beta/v_0$, the Newton method will give robust one-sided convergence to $\hat{t}$. The corresponding impact velocity can then be found from Eq. (23) which is then reversed for the initial data of the second part of the trajectory.

The second piece of trajectory ($\Phi_{\rm B}$) leaves the $\Phi = -\beta$ boundary with known times and velocities $(\hat{t}, -\hat{v})$ and impacts the $\Phi = +\beta$ boundary with unknown times and velocities $(t_1, -v_1)$.

$$\Phi(\hat{t}) = \widehat{c_1} + \widehat{c_2}e^{-\delta\hat{t}} + \varepsilon\cos 2\pi\hat{t} + 4\pi\hat{t} = -\beta, \tag{26}$$

$$\Phi'(\hat{t}) = -\delta\widehat{c_2}e^{-\delta\hat{t}} - 2\pi\varepsilon\sin 2\pi\hat{t} + 4\pi = -\hat{v}, \tag{27}$$

$$\Phi(t_1) = \widehat{c_1} + \widehat{c_2}e^{-\delta t_1} + \varepsilon\cos 2\pi t_1 + 4\pi t_1 = \beta, \tag{28}$$

$$\Phi'(t_1) = -\delta\widehat{c_2}e^{-\delta t_1} - 2\pi\varepsilon\sin 2\pi t_1 + 4\pi = -v_1. \tag{29}$$

If we subtract (26) from (28) and use (27) to substitute for $\widehat{c_2}$, we have

$$\frac{1}{\delta}\left(4\pi - \hat{v} - 2\pi\varepsilon\sin 2\pi\hat{t}\right)\left(e^{-\delta(t_1-\hat{t})} - 1\right) + \varepsilon(\cos 2\pi t_1 - \cos 2\pi\hat{t}) + 4\pi(t_1 - \hat{t}) - 2\beta = 0, \tag{30}$$

to solve for t_1, for which the convergence issues are similar to those for case (a) discussed above. Note that for small δ, the trajectory is approximately reversible in time and hence $2\hat{t} - t_0$ constitutes a good initial guess for t_1. Once t_1 is found, the corresponding impact velocity v_1 is given by Eq. (29).

We have now constructed a complete map P for the impacting contact model Eqs. (4,5), and we proceed to construct a similar map for the piecewise linear model Eqs. (1,2).

3 Construction of P for the Piecewise Linear Model

To calculate the Poincaré map P for the piecewise linear model we can adapt the impact map described above by replacing elastic impacts with the backlash boundaries with excursions into one of the linear stiffness regimes. We refer to the $\Phi \geq +\beta$ regime as *linear contact*, and the $\Phi \leq -\beta$ regime as *torque reversal*. As before we construct a map in time and velocity at the point of departure ($\Phi' < 0$) from the $\Phi = +\beta$ boundary to the next such departure, noting attraction to permanent linear contact if no such departure exists.

In contrast to the impacting contact model, where the robustness of our numerical procedures can be guaranteed, here we have to proceed by formal arguments which nevertheless appear to converge to the correct root in all cases that we have examined. Details of proofs have not been attempted.

Consider a trajectory with initial data $-\beta < \Phi \leq +\beta$ and $\Phi' < 0$. As before, such a trajectory must impact either $\Phi = +\beta$ or $\Phi = -\beta$ at some subsequent time. We note that any crossing of

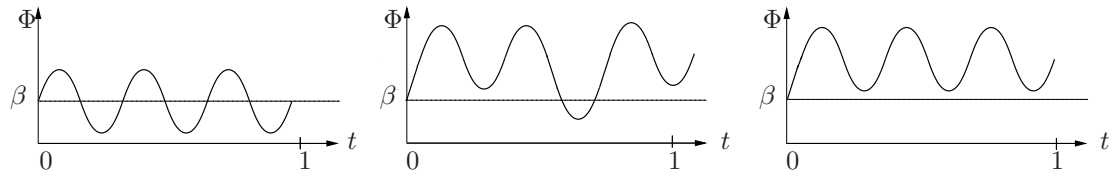

Figure 4: Sketches of three example trajectories departing from $\Phi = +\beta$ with $\Phi' > 0$. From left to right: (a) the trajectory oscillates between linear contact and freeplay, (b) trajectory returns to freeplay (within one gross rotation) after several maxima and minima in linear contact, (c) the trajectory stays in permanent linear contact.

the $\Phi = -\beta$ boundary from freeplay must be followed by another crossing of $\Phi = -\beta$ back into freeplay, by the following argument.

At a turning point $\Phi' = 0$ in $\Phi \leq -\beta$ we have

$$\Phi'' = -2\kappa\beta + 4\pi\delta - 2\kappa\Phi - 2\pi\varepsilon(4\pi^2 + \delta^2)^{\frac{1}{2}} \cos(2\pi t + \xi), \tag{31}$$

where ξ is a phase shift. This expression is always positive provided

$$\varepsilon < \frac{2\delta - (\beta + \Phi)}{(4\pi^2 + \delta^2)^{\frac{1}{2}}}. \tag{32}$$

Since Eq. (3) holds and $\Phi \leq -\beta$ in this regime, this bound is always satisfied and there can be no local maxima in the torque reversal regime.

Let us now consider trajectories where $\Phi > +\beta$ and $\Phi' > 0$, i.e., a trajectory in the linear contact regime with positive velocity. There can be many maxima and minima of Φ before the trajectory re-crosses the $\Phi = +\beta$ section and returns to the freeplay region, if it in fact does ever return. We assume that if a trajectory does not re-cross $\Phi = +\beta$ within one gross rotation that it will never re-cross and it will remain in the linear contact regime for all time, i.e., permanent linear contact. Some example trajectories with initial data $\Phi = +\beta$ and $\Phi' > 0$ are illustrated in Fig. 4.

To locate exit points from the linear contact regime, and hence re-crossings of $\Phi = +\beta$, we must first find the maxima (and minima, if any) within it. Unfortunately, it is not possible to find these maxima and minima in closed form. However, we can calculate good approximations, motivated by the relative sizes of terms, as outlined below.

The general solution of Eq. (1) in the linear contact regime has the form

$$\Phi(t) = \sqrt{A^2 + B^2} e^{-\frac{\delta t}{2}} \cos(qt + \zeta) + \beta + \frac{2\pi\delta}{\kappa} + p\cos(2\pi t + \lambda), \tag{33}$$

where A and B are constants of integration which can be expressed in terms of the initial conditions, and

$$\zeta = \arctan\left(-\frac{A}{B}\right), \tag{34}$$

$$q = \sqrt{2\kappa - \frac{\delta^2}{4}} \approx \sqrt{2\kappa}, \tag{35}$$

$$p = -\pi\varepsilon\sqrt{\frac{4\pi^2 + \delta^2}{(\kappa - 2\pi^2)^2 + \pi^2\delta^2}} \approx -\frac{2\pi^2\varepsilon}{\kappa}, \tag{36}$$

$$\lambda = \arctan\left(\frac{\delta(\kappa - 2\pi^2) - 2\pi^2\delta}{\pi\delta^2 - 2\pi(\kappa - 2\pi^2)}\right) \approx -\frac{\delta}{2\pi}. \tag{37}$$

To determine if an exit from the linear contact regime is possible we must find the turning points of Eq.(33). We require $t_{\rm m}$ such that $\Phi'(t_{\rm m}) = 0$, i.e.,

$$-q\sqrt{A^2+B^2}e^{-\frac{\delta t_{\rm m}}{2}}\sin(qt_{\rm m}+\zeta) - \frac{\delta}{2}\sqrt{A^2+B^2}e^{-\frac{\delta t}{2}}\cos(qt_{\rm m}+\zeta) - 2\pi p\cos(2\pi t_{\rm m}+\lambda) = 0. \quad (38)$$

Eq. (38) cannot be solved in closed form. However, if we examine both the frequencies and amplitudes of the three sinusoidal terms we can identify the leading order terms. We note that the first two terms of Eq. (38) oscillate significantly faster, $O(\sqrt{\kappa})$ than the third term, $O(1)$ and hence there is a decoupling of time scales. In addition, the amplitude of the first term, is proportionately considerably larger than that of the second, by a ratio $O(\sqrt{\kappa})$ to $O(\delta)$.

Hence, as a good approximation to the solution of Eq. (38) we solve:

$$\sin(qt_{\rm m}+\zeta) = 0, \quad (39)$$

$$\Rightarrow t_{\rm m} = \frac{m\pi-\zeta}{q}, \quad (40)$$

where $m \in \mathbb{Z}$. Equation (40) is a maximum of Eq. (33) if m is odd and a minimum if m is even.

We can then use t_m to to determine if a crossing of $\Phi = +\beta$ exists within one gross rotation (namely if there exists a $\Phi(t_m) < +\beta$ with m even) and further to bracket such a crossing. Due to the possibility of multiple crossings of $\Phi = +\beta$, we cannot guarantee that Newton's method will locate the correct (i.e. the first) root, and hence we employ instead a combination of interval bisection and secant methods. That is, we use Eq. (40) to approximate the first minimum of $\Phi < +\beta$, as well as the previous maximum, which together bracket the root. Equation (33) then gives the exact values of Φ' at the interval endpoints; if both are negative the secant method should locate the crossing of $\Phi = +\beta$ with superlinear convergence. If the gradients are of different sign, however, we can use interval bisection until the gradients are of the same sign; the secant method can then be applied with confidence.

A similar method can be used to find the minimum in $\Phi \leq -\beta$ to locate an initial guess for the exit point from the torque reversal regime.

Our method (for initial conditions departing from $\Phi = +\beta$ with negative velocity) can be summarised as follows.

- Identify whether the the next crossing is with $\Phi = +\beta$ or $\Phi = -\beta$ using the pre-computed grazing curve.
- If the next crossing is with $\Phi = -\beta$:
  - Locate the next crossing of $\Phi = -\beta$ using the Poincaré map for the impacting contact model.
  - Approximate the minimum that occurs in $\Phi \leq -\beta$.
  - Temporarily neglect the existence of the freeplay region, and approximate the next maximum (note that this maximum is non-physical)
  - The root of $\Phi = -\beta$ is bracketed by this minimum and the maximum.
  - Apply the secant method to locate the crossing.
- Use the Poincaré map for the impacting contact model to locate the next crossing of $\Phi = +\beta$.
- To determine whether the trajectory remains in permanent linear contact, or not:
  - Temporarily neglect the existence of the freeplay region, and approximate the first minimum that occurs in $|\Phi| < \beta$ within one gross rotation (note that this minimum is non-physical). If there is no such minimum this initial condition is marked as one that results in PLC.

– Approximate the previous maximum.
– The root of $\Phi = +\beta$ is bracketed by this minimum and the maximum.
– Use Eq. (33) to find the exact gradients of Φ at the interval endpoints.
– If the gradients of both points are negative, use the secant method to locate the crossing of $\Phi = +\beta$.
– If the gradients at these points are of different signs, use interval bisection until the new endpoints are both negative. Apply the secant method to locate the crossing.

Having constructed the Poincaré map P for the full piecewise linear model Eqs. (1,2), in addition to that for the impacting contact model, Eqs. (4,5), we now proceed to describe how they are used to compute the basins of attraction of solutions of these models.

4 Cell-to-Cell Mapping in Nonsmooth Systems

Our objective is to calculate the basins of attraction of both the full piecewise linear (Eqs. (1,2)) and impacting contact (Eqs. (4,5)) gear rattle models, by the brute-force simulation of a large number of initial conditions. To this end, we employ the method of *cell-to-cell mapping* [Hsu and Guttalu, 1980; Hsu, 1987], applied to the Poincaré maps P defined in Secs. 2 and 3. The region of interest (in this instance a closed bounded subset of the domain of P, namely the time and velocity (t, v) of departures from $\Phi = +\beta$) is divided into a uniform rectangular grid of cells, where each cell has a unique cell number associated with it.

The centre point of each cell (t^c, v^c) corresponds to one set of initial data. The dynamics of the system are described by a mapping, in our case the Poincaré map $P : (t_i, v_i) \mapsto (t_{i+1}, v_{i+1})$. This mapping can then be applied to each initial condition to yield a 'cellular' form of the Poincaré map, which we call a *cell-map* $P_{\text{cell}} : (t_i^c, v_i^c) \mapsto (t_{i+1}^c, v_{i+1}^c)$ which maps cell-centres to cell-centres (or, equivalently, cells to cells). The cell-map is a composition of the Poincaré map P, and a 'correction' map P_{corr} that maps points to the nearest cell-centre (see Fig. 5(a)). We now know to which cell in the grid each initial condition maps. The implicit assumption is that all points within a given cell map to the same cell; a finer grid gives better accuracy, but requires more computation. In principle, as we let the cell-size tend to zero, the cell-map will converge to the Poincaré map itself.

As there are a finite number of cells in this framework, every cell in the cell-map is either a periodic attractor or maps outside the grid. One implication of this is that chaotic solutions cannot be directly identified, but can be inferred as being solutions of large period, which increases as cell-size tends to zero.

Solutions with small damping, δ, as is characteristic for the systems we study, suffer from particularly long transients. In order to determine the long term behaviour we adapt Hsu's method. We apply the Poincaré map to each initial condition and record the terminal positions. We then repeat this procedure many times using the 'uncorrected' terminal points as the new starting conditions. That is, we compute $P_{\text{corr}}(P^k(t^c, v^c))$, rather than $P_{\text{cell}}^k(t^c, v^c)$; see Fig. 5(b). This method is akin to long time integration to eliminate transients but is computationally much cheaper, yet more accurate than a simple iteration of the cell-map. We need to be careful in choosing the number of applications, k, of the Poincaré map to ensure that the correct periodicity is calculated. A simple way to do this, without the need for any extra computer code, is to choose k to be a large prime number. In this way the true periodicity of each basin of period less than k (from the point of view of the cell-map) is calculated.

To extract efficiently the global properties from the mapping, algorithms described in [Hsu and Guttalu, 1980; Hsu, 1987] can be employed to determine all the information that we require for

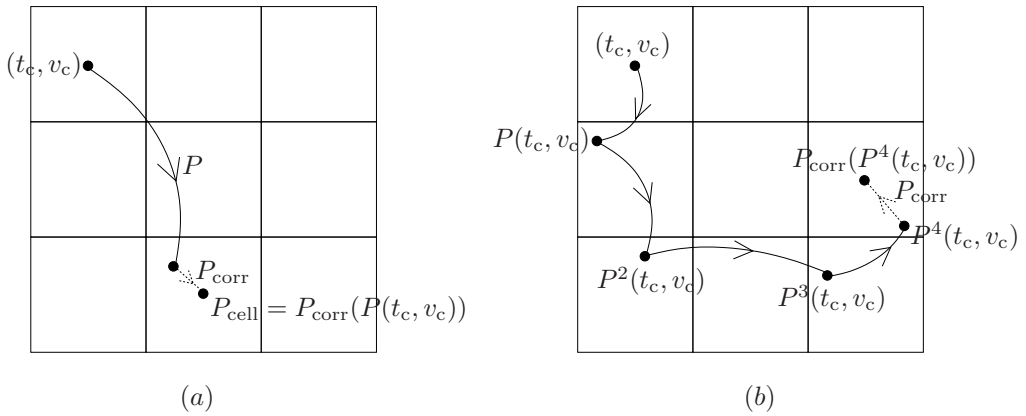

Figure 5: Schematic illustrations of (a) the cell-map P_{cell}, and (b) the map we use to minimise the effect of long transients $P_{\text{corr}} \circ P^k$, where the Poincaré map P is applied k times (here $k = 4$) followed by the correction map, P_{corr} to re-centre the terminal point.

constructing the basins of attraction. For each cell there are three possibilities: the cell is a *periodic cell*, i.e., this cell belongs to a periodic orbit; the cell is mapped outside the grid, or the cell is mapped into a periodic cell. For each cell the algorithm assigns: a group number (basin number), a periodicity number (the number of impacts of $\Phi = +\beta$ before the trajectory repeats itself), and a step number (the number steps of it takes to map this particular cell into a periodic cell). Note that there are as many group numbers as there are periodic orbits, and that a step number of zero implies a periodic cell.

In what follows, we will use the cell-to-cell mapping technique to explore the solution of the gear-rattle models by computing their basins of attraction. For the purposes of visualisation, we colour each basin according to its itinerary, i.e., the pattern of impacts that occur with both backlash boundaries. Shorter itineraries are represented by shorter wavelength (bluer) colours. At the two extremes of the colour scale; dark blue denotes behaviour akin to permanent linear contact and red, chaotic behaviour. This results in a uniform colour scale across the results below; the same colour in more than one picture denotes the same solution type.

To identify the many different periodic solutions, we use the notation introduced in [Halse et al., 2007] to identify some different types of periodic solution. We let $P(m, n^+, n^-)$ denote a periodic solution, of period $m \in \mathbb{Z}$, where $n^{\pm}$ denote the number of times per period that the orbit impacts/crosses the $\Phi = \pm\beta$ boundaries respectively. Whilst this notation is useful it does not classify all solution types, or identify the order in which impacts of $\Phi = +\beta$ and $\Phi = -\beta$ occur.

It is important to emphasise here the subtle difference between periodicity and impact periodicity. As we use an impact-based map, the periodicity that we calculate is the impact periodicity; this is the number of times the trajectory impacts $\Phi = +\beta$ before repeating. For example, in one time period $t \in [0, 1]$ a solution may impact $\Phi = +\beta$ twice (with different velocities) before repeating, therefore having an impact periodicity of two.

5 Basins of Attraction Computations

To investigate changes in the dynamics of the gear rattle models as system parameters are varied, we perform three sets of numerical experiments: we vary stiffness, eccentricity and damping in turn, and observe how the existence of solutions changes, by producing basins of attraction and bifurcation diagrams. Each basin of attraction plot presented in this section (Figs. 6–10 and

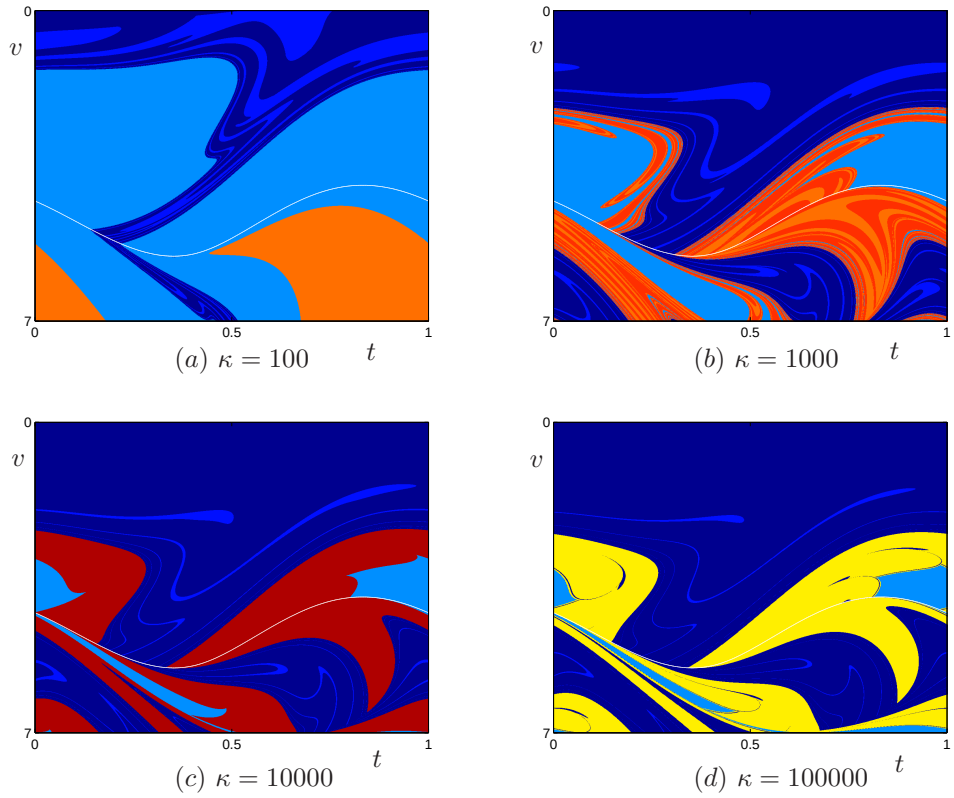

Figure 6: Basins of attraction for the piecewise linear model, Eqs. (1,2), when $\delta = 0.6$, $\beta = 0.6$, $\varepsilon = 0.1$ and varying stiffness κ (indicated below each panel). Each plot has time on the x-axis and velocity on the y-axis. The grazing curve is overlaid in white. Computations were performed using the cell-to-cell mapping techniques described in Sec. 4.

Figs. 12–16) illustrates the cell map $P_{\text{corr}} \circ P^k$ computed on a regular grid of 1000×1000 cells, each cell representing a different initial condition. As described above, k is chosen to be a large prime; here we use $k = 1499$, as we find that using a larger prime does not result in any visible changes in the basins. In each case, the grazing curve is overlaid in white, and the scale is chosen so that transitions either side of the grazing curve can be observed.

5.1 Varying stiffness

We begin by examining the effect of varying stiffness κ in the piecewise linear model, Eqs. (1,2), with fixed damping $\delta = 0.6$, eccentricity $\varepsilon = 0.1$, and backlash $\beta = 0.6$. We have chosen these parameters as scaled-up versions of the realistic machine parameters. The results of these computations are shown in Fig. 6; we show the basins of attraction where stiffness changes by an order of magnitude between each panel, increasing from $\kappa = 100$ to $\kappa = 100000$.

We also compare the dynamics of the piecewise linear model, Eqs. (1,2), and impacting contact model Eqs. (4,5), at the same values of δ, β and ε. The basins of attraction are shown in Fig. 7, for both models, when the stiffness has been taken to be an order of magnitude bigger again ($\kappa = 1000000$). Fig. 7 also illustrates several common solution types under the two different models:

- PLC solutions are represented in dark blue.

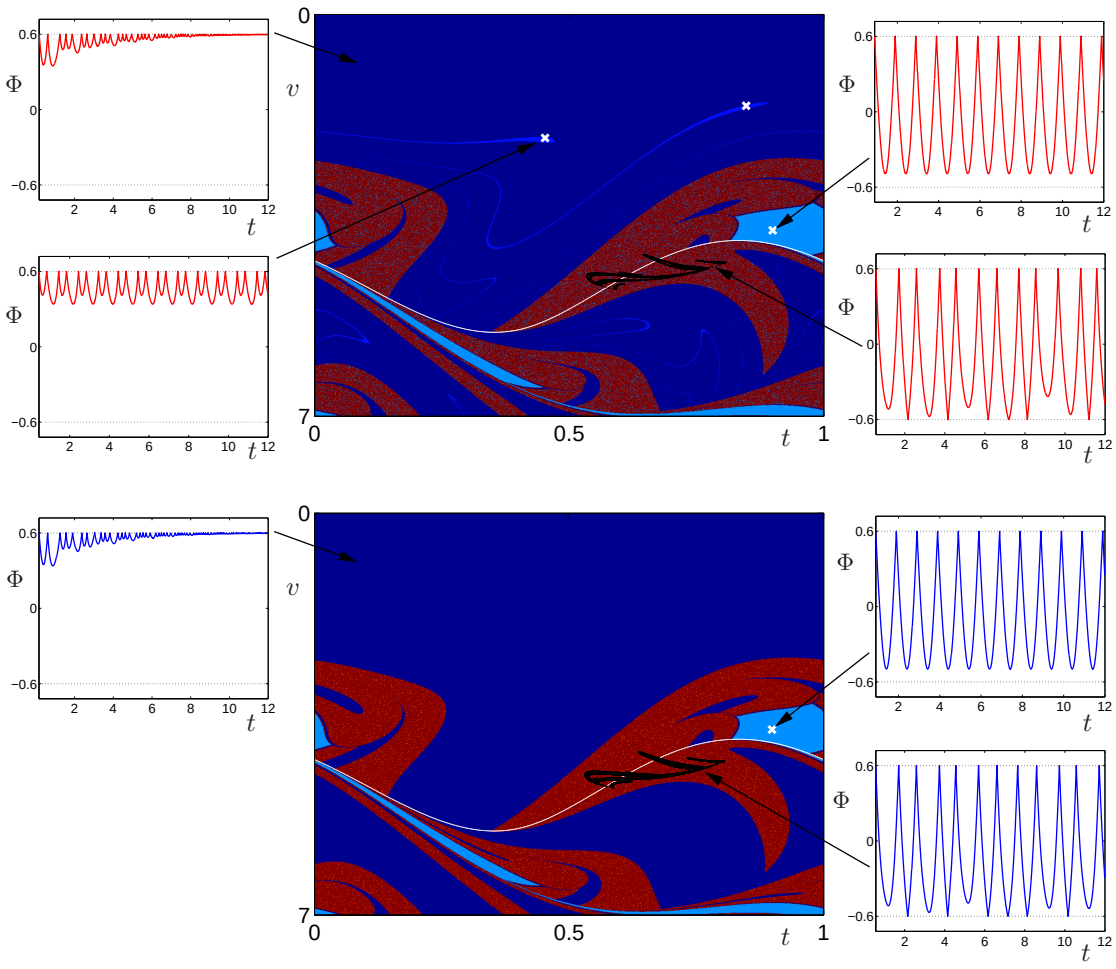

Figure 7: Basins of attraction for the PWL model (top) Eqs. (1,2) and impacting contact model (bottom) Eqs. (4,5). In both models $\delta = 0.6$, $\beta = 0.6$, $\varepsilon = 0.1$, and for the PWL model $\kappa = 1 \times 10^6$. The periodic and chaotic attractors are overlaid on the basins in white ($\times$) and black respectively. Time histories, $\Phi(t)$ versus t, of the periodic and chaotic attractors for both models are illustrated next to the corresponding basin of attraction.

- A chaotic region is shown in speckled dark red.
- A basin of $P(1,1,0)$ solutions, very close to grazing, is shown in pale blue.
- A basin of $P(1,2,0)$ solutions, which is revealed only by the PWL model, is shown in blue.

The time histories of these solutions are all labelled with arrows. The periodic attractors are overlaid on the basins of attraction in white ($\times$). To generate the chaotic attractors (since these cannot be directly identified using cell-to-cell mapping) we repeatedly apply the Poincaré map to an initial condition in the chaotic regime, remove the transients, and plot the impact times and velocities on the basin of attraction in black.

We observe from Fig. 7 that the basins of attraction for the impacting contact model and full piecewise linear model as $\kappa \to \infty$ are very similar, except for one small basin as already noted. In the case of the impacting contact model, the basin of PLC solutions is replaced by one where the solution has multiple, very low velocity impacts with $\Phi = +\beta$. Fig. 6 shows that the qualitative agreement between the PWL and the impacting contact models improves as κ increases. We shall therefore exclusively work with the impacting contact model for the remainder of this paper. We defer the full analysis of the differences between two models for future work.

5.2 Varying eccentricity

We now go on to examine the effect of varying eccentricity ε in the impacting contact model Eqs. (4,5) with fixed damping $\delta = 0.6$ and backlash $\beta = 0.6$. The results of these computations are shown in Fig. 8; we show the basin of attraction plots where eccentricity increases in increments of 0.0055 from 0.056 to 0.1.

We note that although the PLC bound, Eq. (3), is satisfied, there are several coexisting solutions. As ε decreases, the dynamics decrease in complexity as expected. At $\varepsilon = 0.067$ (Fig. 8(c)) there are only two basins, corresponding to solutions which repeatedly impact $\Phi = +\beta$ with very low velocity (akin to PLC) and solutions of type $P(1,1,0)$. As ε decreases further the basin of $P(1,1,0)$ solutions shrinks until it completely disappears and PLC takes over. This occurs at the predicted bound for the existence of $P(m,1,0)$ solutions,

$$\varepsilon > \frac{m^2\delta^2}{6} - \frac{m^4\delta^4}{360} + O(\delta^6), \tag{41}$$

computed in [Halse et al., 2007; Mason et al., 2007]. Substituting the values of ε and δ used in the simulation we find the bound for the existence of $P(1,1,0)$ solutions, $\varepsilon > 0.05964$, is in good agreement with our results, see Fig. 8. However, in practice ε and δ are of similar magnitude, and it is very difficult to eliminate rattling solutions by reducing eccentricity.

5.3 Varying damping

We now proceed to examine the effect of varying damping in the impacting contact model Eqs. (4,5) with fixed eccentricity $\varepsilon = 0.1$ and backlash $\beta = 0.6$. The results of these computations are shown in Fig. 8; we show the basin of attraction plots where damping increases in increments of 0.025 from 0.5 to 0.7.

We make several observations:

- The plots decrease in complexity as damping increases until all initial conditions result in behaviour akin to PLC, as in Fig. 9(i).

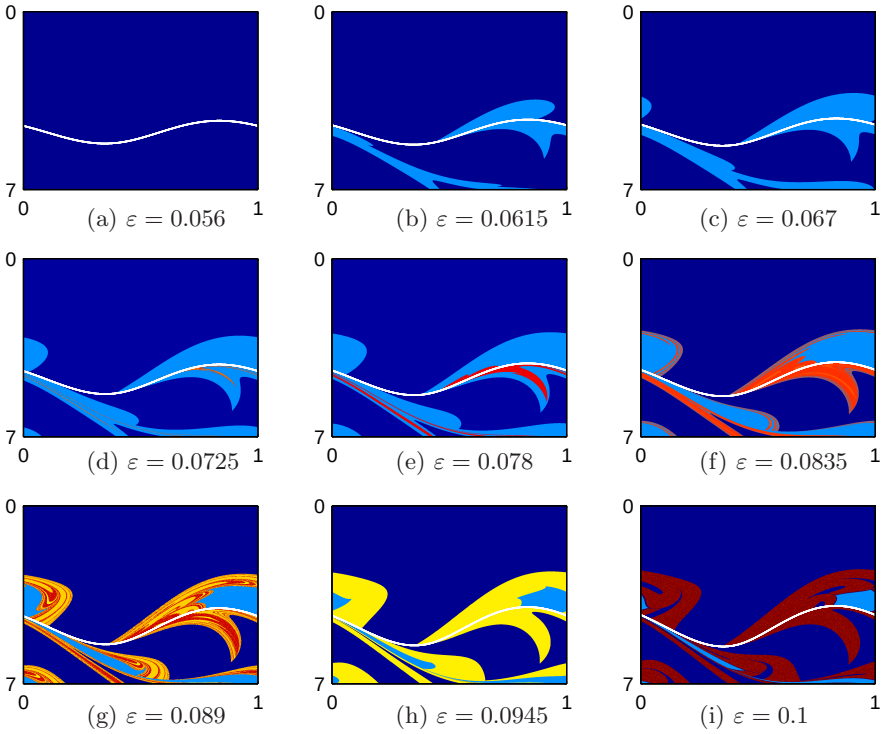

Figure 8: Basins of attraction for the impacting contact model, Eqs. (4,5), for $\delta = 0.6$, $\beta = 0.6$ and varying eccentricity, between $\varepsilon = 0.056$ and $\varepsilon = 0.1$. Each plot has time on the x-axis and velocity on the y-axis. In case (a) all initial conditions result in behaviour akin to permanent linear contact.

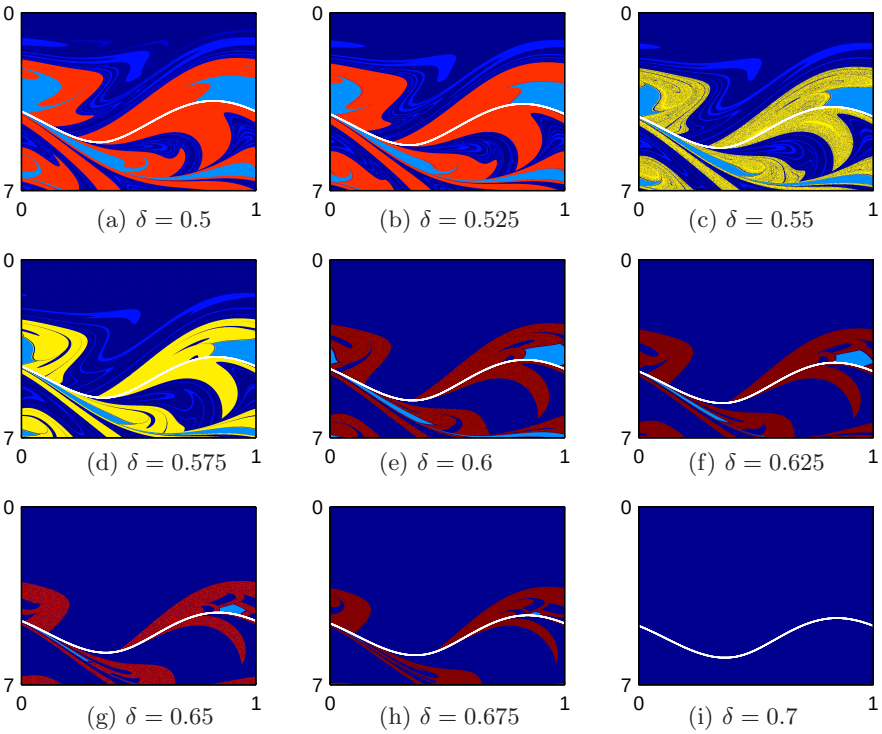

Figure 9: Basins of attraction for the impacting contact model, Eqs. (4,5), for $\beta = 0.6$, $\varepsilon = 0.1$ and varying damping, between $\delta = 0.5$ and $\delta = 0.7$. Each plot has time on the x-axis and velocity on the y-axis. In case (i) all initial conditions result in behaviour akin to permanent linear contact.

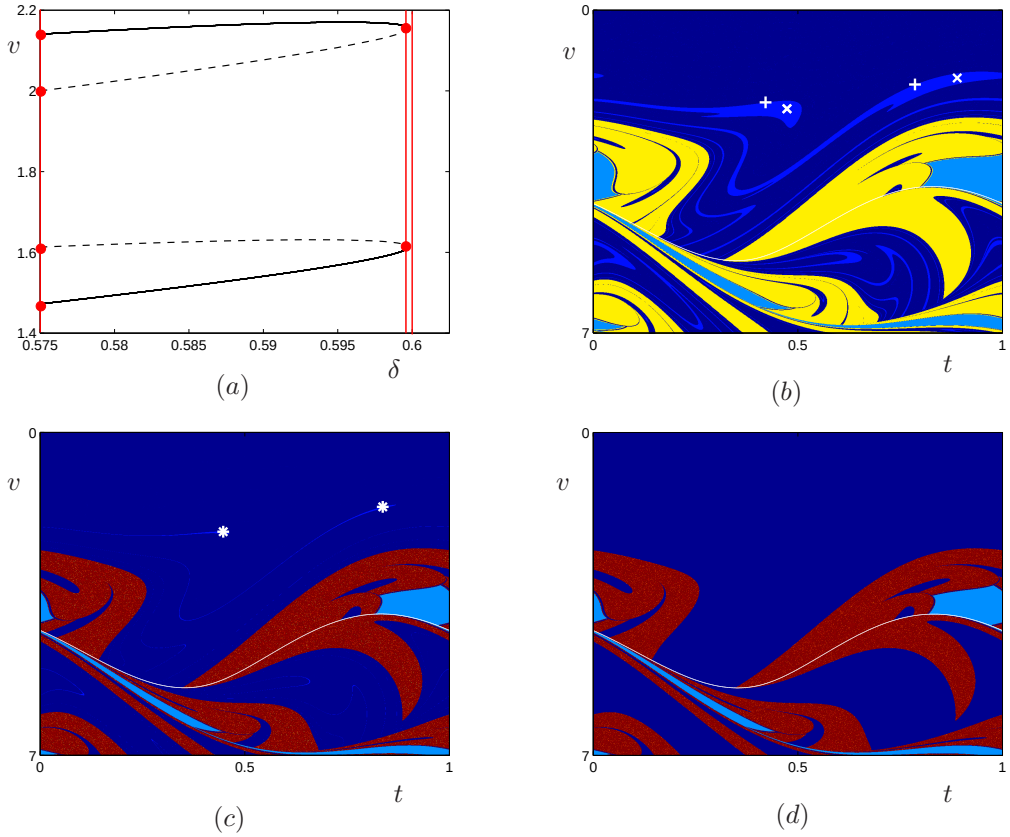

Figure 10: (a) Bifurcation diagram of a $P(1,2,0)$ solution, in the impacting contact model, Eqs. (4,5), of impact velocity against damping, for fixed $\beta = 0.6$ and $\varepsilon = 0.1$. As damping increases this solution is destroyed in a saddle-node bifurcation at $\delta = 0.5997$ (the stable and unstable branches are plotted in solid and dashed lines respectively). Basins of attraction (b) before, (c) at, and (d) after the saddle-node bifurcation. The attracting and saddle-type $P(1,2,0)$ solutions ($\times$ and $+$ respectively) are overlaid. As damping increases these move closer to each other until they collide in a saddle-node bifurcation (c) at $\delta = 0.5997$. (d) The basin is destroyed by $\delta = 0.6$.

- As damping increases, between $\delta = 0.575$ (Fig. 9(d)) and $\delta = 0.6$ (Fig. 9(e)), a solution of type $P(1,2,0)$ is destroyed. Similarly between $\delta = 0.5$ (Fig. 9(a)) and $\delta = 0.525$ (Fig. 9(b)), a $P(1,3,0)$ orbit is destroyed.
- The chaotic region in Fig. 9(e), in speckled red, that we illustrated earlier, see Fig. 7, is periodic for lower values of damping, e.g. in Fig. 9(b) (orange) and Fig. 9(d) (yellow).

To understand some of the mechanisms by which solutions are created and destroyed, we plot one-parameter bifurcation diagrams of impact velocity, v, as damping, δ, is varied. To generate these bifurcation diagrams the Poincaré map is applied to an initial condition many times, and for each damping value the last twenty impact velocities are plotted. To ensure that the same orbit is followed we use 'pseudo continuation': the time and velocity at impact from value of δ are used as the initial conditions for the next value of δ.

Initially, we investigate the basin that disappears between $\delta = 0.575$ and $\delta = 0.6$. In Fig. 10(a) we plot both the $P(1,2,0)$ attractor and saddle in red at $\delta = 0.575$. We apply the continuation-type method to the impact time and magnitude of velocity at the attractor. By increasing damping (until $\delta = 0.6$) we obtain two branches of solutions which we plot in solid black lines. The location

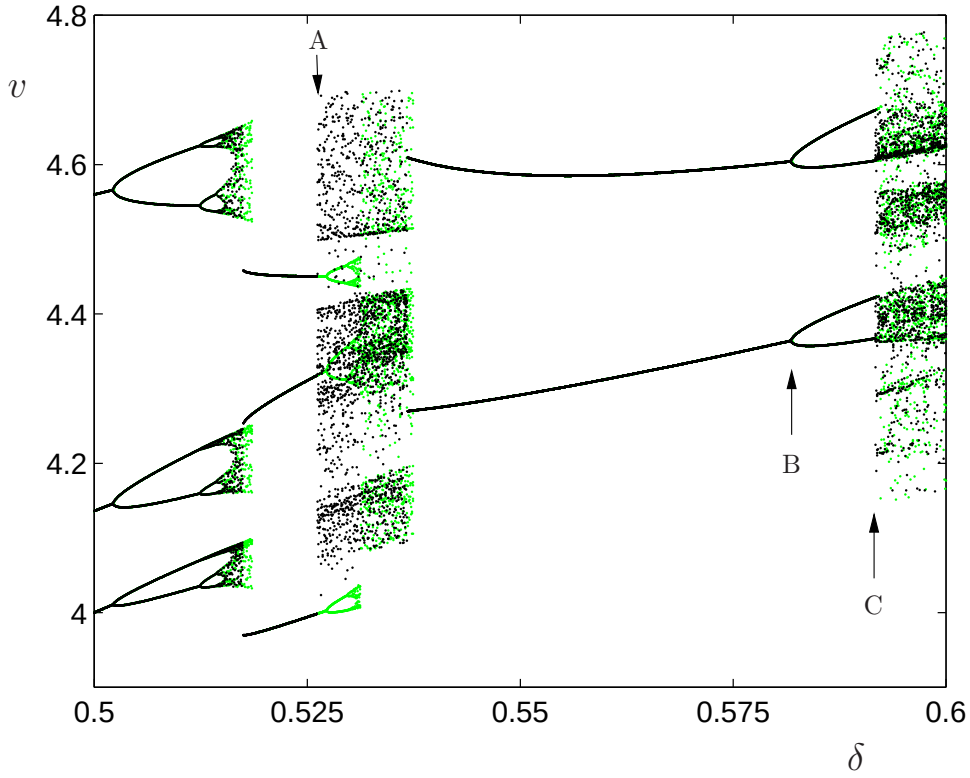

Figure 11: Bifurcation diagram of impact velocity against damping for the impacting contact model, Eqs. (4,5) , for $\beta = 0.6$ and $\varepsilon = 0.1$, plotted for increasing (green) and decreasing (black) δ. An example of coexisting attractors is labelled at (A). Examples of period-doubling and a grazing bifurcation are labelled at (B) and (C) respectively.

of the saddle as damping is varied is calculated using DsTool (Dynamical Systems Toolkit) [Back et al., 1992] and its branch is plotted as dashed black lines. At $\delta = 0.5997$ we find a saddle-node bifurcation, i.e., a collision of the attractor and unstable saddle, resulting in the destruction of this orbit and the disappearance of this basin. The basins of attraction before, at, and after the saddle-node bifurcation are also shown in Figs. 10(b), 10(c) and 10(d) respectively, with attractors ($\times$) and saddles ($+$) overlaid.

We now examine how the $P(3, 3, 2)$ periodic orbit that exists at $\delta = 0.5$, with basin of attraction coloured orange in Fig. 9(a), changes as δ increases. We apply the continuation-type method described above, increasing δ until $\delta = 0.6$, and plot the magnitude of the velocity of departure from $\Phi = +\beta$ after transients have died away for successive values of δ; shown in green in Fig. 11. We then apply the same continuation method in reverse, using the final impact time and velocity at $\delta = 0.6$, decreasing δ until $\delta = 0.5$. The magnitude of the velocity of departure is overlaid on Fig. 11 in black. We observe coexisting solutions (e.g. at A) as well as both period-doubling (e.g. at B) and discontinuity-induced bifurcations (e.g. at C). We proceed to investigate points A, B and C in more detail.

At $\delta = 0.527$, marked as A on Fig. 11, there is a chaotic attractor (black) which coexists with a $P(3, 3, 2)$ attractor (green). The basins of attraction at this value of δ are plotted in Fig. 12(a). The coexisting attractors are depicted as intertwined dark and light orange basins, and their corresponding time histories are shown in Figs. 12(b) and 12(c).

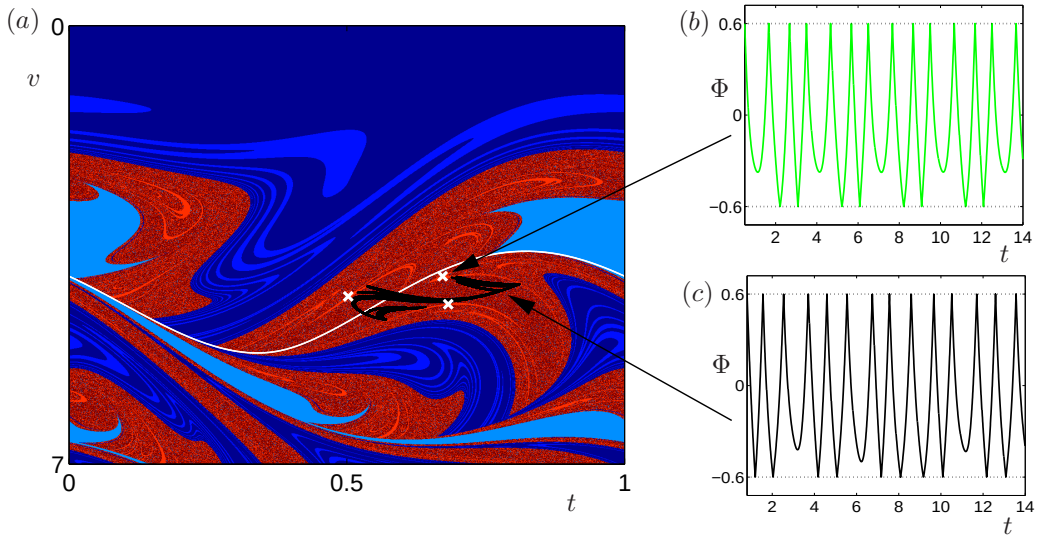

Figure 12: (a) Basins of attraction for the impacting contact model, Eqs. (4,5), when $\delta = 0.527$, $\beta = 0.6$, $\varepsilon = 0.1$. A $P(3,3,3)$ and a chaotic attractor are overlaid on the basins in white ($\times$) and black respectively. Time histories, $\Phi(t)$ versus t, of (b) stable $P(3,3,2)$ periodic motion (light orange basin), and (c) the coexisting chaotic motion (dark orange basin).

Finally, we examine the $P(2,2,1)$ periodic orbit, at $\delta = 0.575$. This orbit period-doubles at $\delta = 0.5819$ (marked as B on Fig. 11) to become a $P(4,4,2)$ orbit. It then undergoes a discontinuity-induced bifurcation at $\delta = 0.5922$ (marked as C on Fig. 11) where the orbit collides with the grazing curve, to be replaced by the chaotic attractor whose basin surrounds the grazing periodic orbit. Basins of attraction and the time histories (of the attractors described above) for values of δ before and at the discontinuity-induced bifurcation are shown in Figs. 13(a) and 13(b) respectively.

In summary, we have found that small changes in damping can cause a plethora of smooth and discontinuity-induced bifurcations. As damping increases enough, however, we see that all initial conditions result in behaviour akin to permanent linear contact. Despite the desirability of PLC from a machine-design point of view, significantly increased damping is not a viable engineering solution, as power consumption is directly proportional to the damping and hence increasing δ would make a machine more expensive to run. It seems inevitable, therefore, that any design solution will have to take account of the coexistence of different types of rattling solutions, and that the basins of attraction may be a useful tool to help understand their structure.

6 Basin Boundary Computations

Although we have been concerned with time-efficient computation of basins of attraction, they are still expensive to compute. We now explore two alternative methods to gain insight about the location of the basin boundaries for the impacting contact model: calculation of the pre-images of the grazing curves, and the computation of stable manifolds.

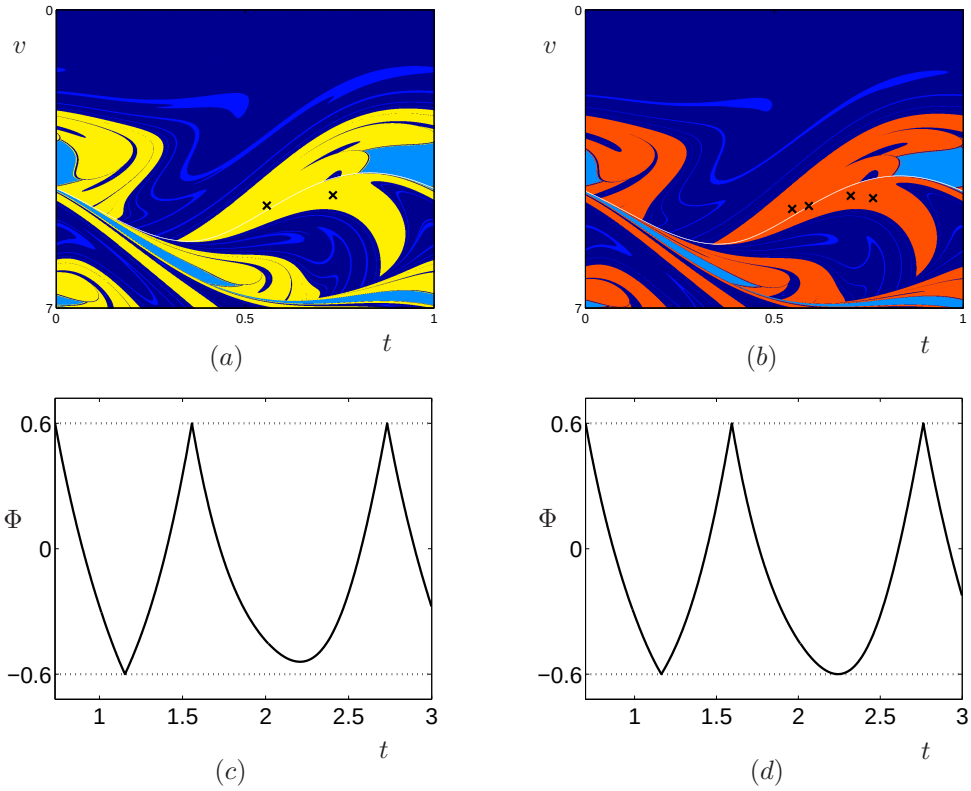

Figure 13: Basins of attraction of the impacting contact model, Eqs. (4,5), with fixed $\beta = 0.6$ *and* $\varepsilon = 0.1$ *and (a)* $\delta = 0.575$ *and (b)* $\delta = 0.5922$*. A* $P(2,2,1)$ *and a* $P(4,4,2)$ *attractor are overlaid on the basins in black (*$\times$*) in (a) and (b) respectively. Time histories,* $\Phi(t)$ *versus* t*, of (c) a stable* $P(2,2,1)$ *solution at* $\delta = 0.575$ *and (d) a grazing* $P(4,4,2)$ *solution at the discontinuity-induced bifurcation at* $\delta = 0.5922$*.*

6.1 Pre-image grazing curves

Much of the intricate structure of the basins of attraction can be explained by the impact-induced discontinuities in the map. These discontinuities can introduce a considerable sensitivity to initial conditions, i.e., a stretching of the phase space, which in particular can be observed around the grazing curve. Other authors have already studied this in detail (see, for example [Budd et al., 1995; Budd and Dux, 1994a,b; Lamba and Budd, 1994]).

Recall that the grazing curve is defined by trajectories that depart $\Phi = +\beta$ at time t with velocity $\Phi' = -v^*$, and whose next contact with $\Phi = \pm\beta$ is a graze with $\Phi = -\beta$ (i.e., with velocity $\Phi' = 0$). We can then define pre-images of this curve in (t, v) space with respect to the Poincaré map P; namely the first pre-image are those initial conditions (t, v) that lead to a graze following one more impact with $\Phi = +\beta$ (possibly via an impact with $\Phi = -\beta$), the second pre-image are those initial conditions (t, v) that graze following two further impacts with $\Phi = +\beta$, and so on.

As an example, in Fig. 14 we overlay the first and second pre-images of the grazing curve for $\delta = 0.6$, $\beta = 0.6$ and $\varepsilon = 0.1$ on the corresponding basins of attraction.

Pre-images of the grazing curve can also provide insight on which initial conditions will eventually be affected by the discontinuity and how the phase space is divided. As previously discussed, the grazing curve acts as a separatrix of trajectories whose next impact is with either $\Phi = +\beta$ or $\Phi = -\beta$. Similar conclusions can be drawn from the pre-image grazing curves. For example the first pre-image consists of two curves. The first piece of curve (above the grazing curve) represents trajectories that initially impact $\Phi = +\beta$, and then graze $\Phi = -\beta$. This acts as a separatrix between trajectories whose second impact is with either $\Phi = +\beta$ or $\Phi = -\beta$.

6.2 Manifold computations

It is well known that for smooth systems, the stable manifolds of saddle points form the basin boundaries [Guckenheimer and Holmes, 1983]. We suspect that this will also be true for our, nonsmooth, system.

First, we locate saddle points using explicit construction techniques described in [Halse et al., 2007; Mason et al., 2007]. We then calculate manifolds numerically using DsTool [Back et al., 1992] with the extension package, Man1D, discussed in [Krauskopf and Osinga, 2000; England et al., 2004]. As an example, we calculate the saddles and corresponding manifolds for $\delta = 0.6$, $\beta = 0.6$ and $\varepsilon = 0.1$. The unstable $P(1, 1, 0)$ saddle can be located analytically, whilst the unstable $P(1, 1, 1)$ saddle is calculated numerically.

In Fig. 15 we overlay the $P(1, 1, 0)$ and $P(1, 1, 1)$ saddles (at A and B) and their corresponding manifolds (magenta and green respectively) on the relevant basins of attraction. We discover that these manifolds do indeed form the basin boundaries, at least to the resolution of our computations.

We now examine the manifold and pre-image curves, and their correspondence with the boundaries of the basins of attraction, more closely. In Fig. 16 we overlay the grazing curve (white), the first and second pre-images of the grazing curve (black and yellow) and the stable manifolds (magenta and green) on a zoomed section of the basin of attraction. We observe that the stable manifolds form the basin boundaries exactly, whilst the grazing curve and its pre-images only approximate some of the locations of the basin boundaries. However, the pre-image grazing curves are cheap to compute as we can use the Newton solvers constructed in Sec. 2 with time reversed. In contrast, computing the stable manifolds requires a good deal more computation. Firstly, the saddles have to be calculated, and secondly DsTool requires the inverse of the Poincaré map as well as the

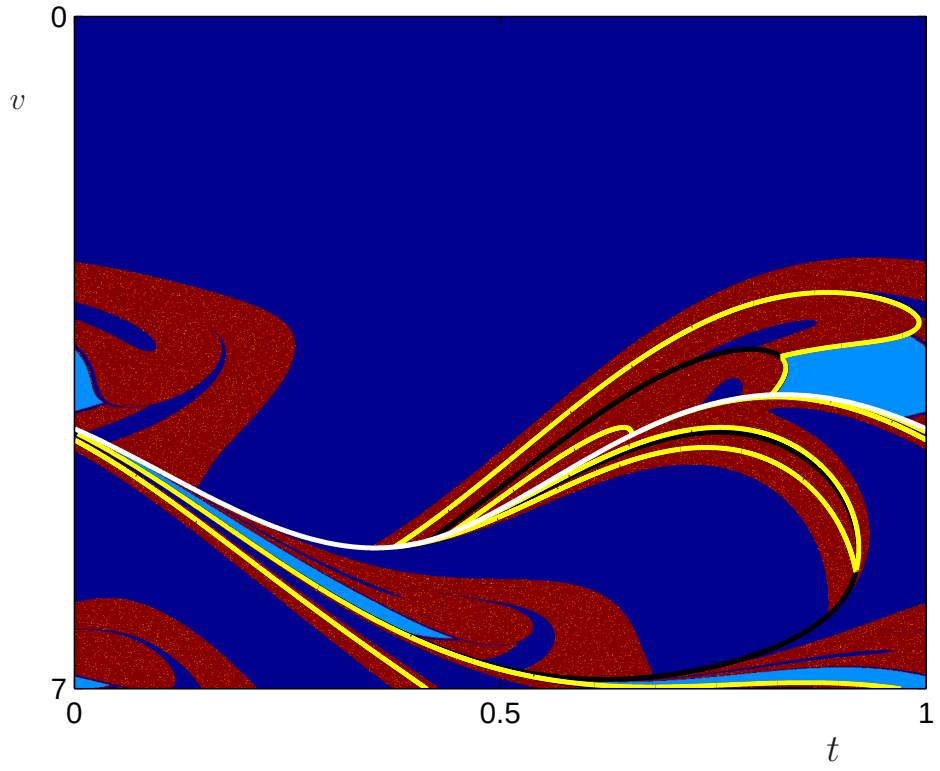

Figure 14: The grazing curve (white) and first and second pre-images of the grazing curve (black and yellow respectively) overlaid on the basin of attraction for the impacting contact model Eqs. (4,5) for $\delta = 0.6$, $\beta = 0.6$ and $\varepsilon = 0.1$. The pre-images were computed using the Newton solvers constructed in Sec. 2 with time reversed.

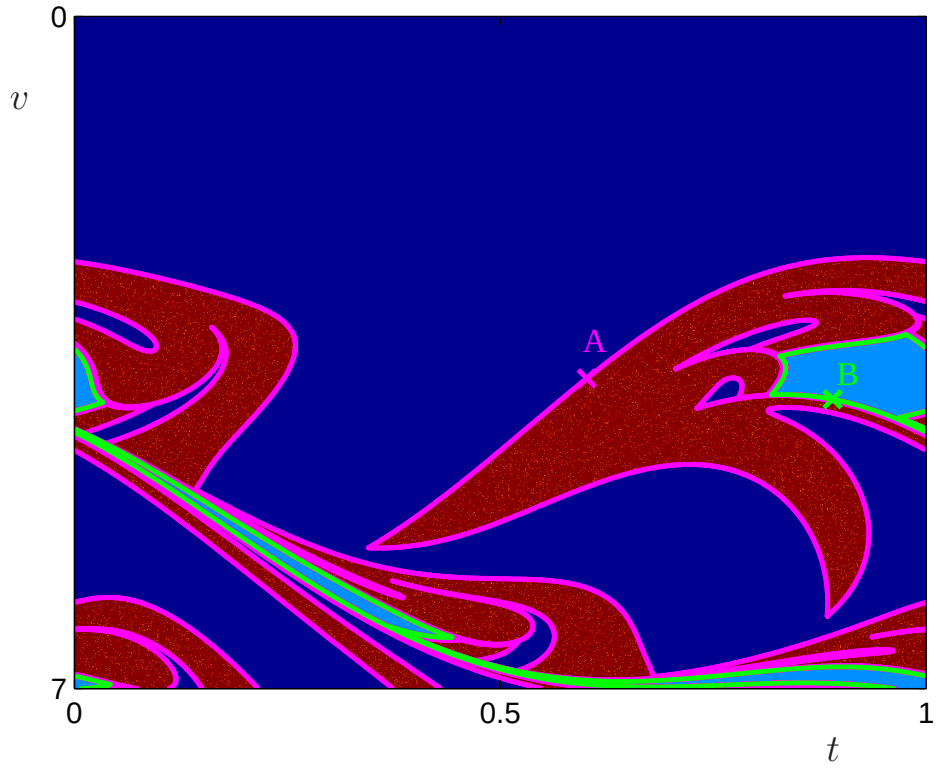

Figure 15: The stable manifolds of the $P(1,1,0)$ saddle at A (magenta) and the $P(1,1,1)$ saddle at B (green) overlaid on the basin of attraction for the impacting contact model Eqs. (4,5) for $\delta = 0.6$, $\beta = 0.6$ and $\varepsilon = 0.1$. The manifolds were generated with DsTool [Back et al., 1992; Krauskopf and Osinga, 2000; England et al., 2004].

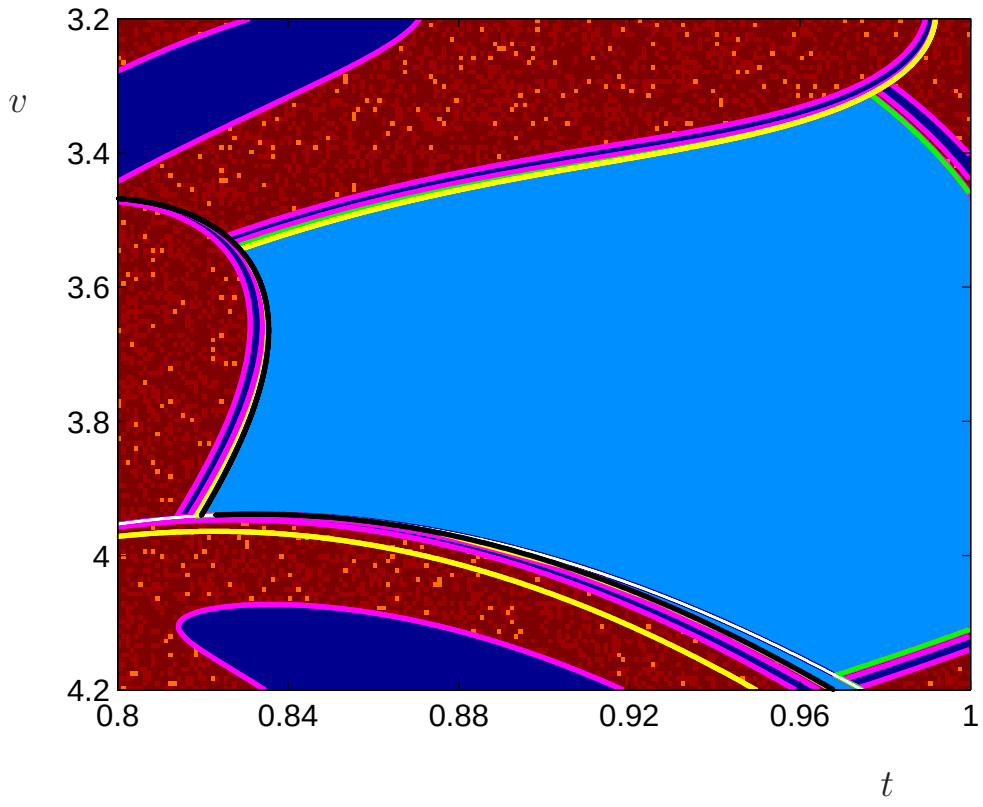

Figure 16: A zoomed section of the grazing curve (white), the first and second pre-images of the grazing curve (black and yellow) and the stable manifolds (magenta and green) overlaid on the basin of attraction for the impacting contact model Eqs. (4,5) for $\delta = 0.6$, $\beta = 0.6$ *and* $\varepsilon = 0.1$.

Poincaré map itself.

If we plot the manifolds over a larger range of v, (Fig. 17) an intricate pattern of stretching and folding is revealed. Trajectories with a high initial velocity gradually lose energy through damping, until they are attracted into the region of interest, $v \in [0, 7]$.

7 Conclusions

In this paper we have examined techniques to efficiently compute basins of attraction for both a (smooth) piecewise linear model and an impacting contact model of a simple one degree-of-freedom backlash oscillator. The application that we have considered is a model of order vibration in gears in lightly-damped quasi-steady operation. We used cell-to-cell mapping techniques to explore how basins change as system parameters are varied. The basins that we have computed reveal complex dynamics with rich and delicate structure. We find stable periodic solutions, and in some cases chaotic regions, that correspond to rattling behaviour. Moreover, these solution types coexist with a quiet solution in which gears remain permanently in contact. The purpose of the basin computation has been to analyse the relative dominance of competing linearly stable solutions in the $t \to \infty$ dynamics.

We have compared the basins of attraction when three key parameters have been varied, namely the

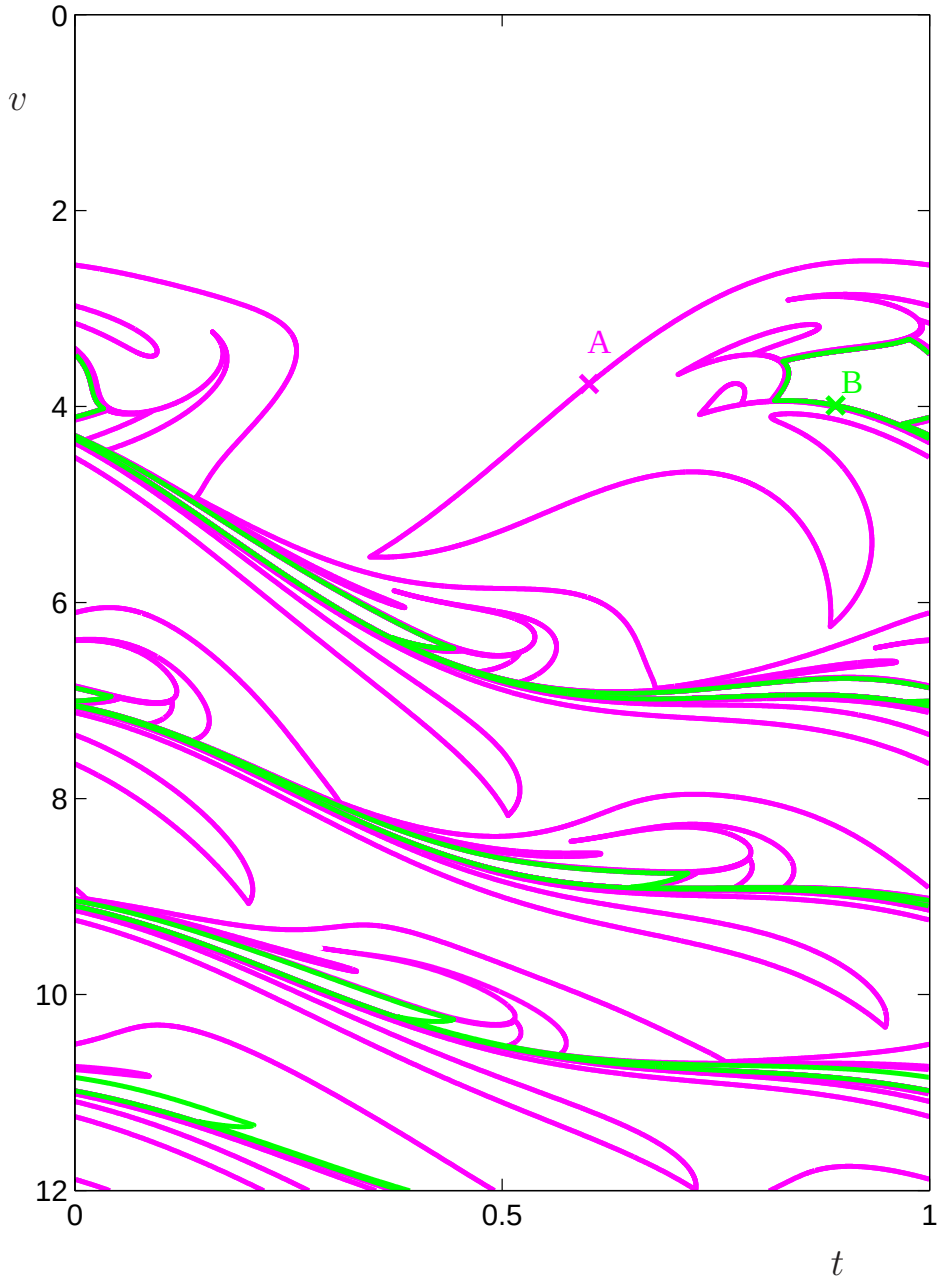

Figure 17: The stable manifolds of Fig. 15 plotted over an extended velocity scale to illustrate the intricate stretching and folding.

stiffness, eccentricity and damping. In the large stiffness limit, we have shown that the impacting contact model is in very good agreement with the full piecewise linear model, validating its use as a computationally efficient scheme. We have found that even small changes in the forcing and damping parameters can give rise to complex dynamics and one-parameter bifurcation diagrams have illuminated some of the key mechanisms for transitions in the system's behaviour. Finally, as eccentricity is reduced, or damping increased, the basin diagrams simplify in structure, and we have shown how the quiet solution, for which gears remain in permanent linear contact, dominates the dynamics.

In addition to the basin computations, we have also computed the grazing curve and its pre-images since these play an important role in the stretching and folding of phase space. Furthermore, we have used DsTool to compute the one-dimensional stable manifolds of saddle point periodic orbits, thus accessing basin boundaries directly. We have found that the stable manifolds and grazing curves wind round each other in interesting ways which are worthy of further investigation from a theoretical point of view. Furthermore, nonsmooth numerical bifurcation tools (e.g., the TC-HAT [Thota and Dankowicz, 2007] extension to AUTO) could be applied to obtain a more detailed understanding of the bifurcations of periodic orbits themselves.

Finally, from the point of view of applications such as the Roots blower vacuum pump, we need to extend the work presented here to deal with much smaller values of damping and forcing, and this presents a significant computational challenge. Preliminary computations have indicated a much more intricate picture: basins diminish in size and more periodic orbits are created (through saddle-node bifurcations) as parameters are decreased.

In Sec. 1, we noted that some real geared systems exhibit noisy operation only intermittently. Our basin of attraction diagrams indicate that only a small change in the initial data is required to move from a basin that corresponds to quiet operation to a basin that corresponds to rattle. A sufficiently large disturbance, which could be caused by any number of external factors, provides one possible explanation for the observed intermittency. From a practical perspective it would be interesting to see if there is a viable method of reducing the machine's sensitivity to perturbations.

Acknowledgements

We thank Howell Jordan for patiently reading and commenting on earlier drafts, Arne Nordmark for fruitful discussions, and Hinke Osinga, Bernd Krauskopf, Clare Judd and James Rankin for help and encouragement with DsTool. JM gratefully acknowledges the support of a CASE award from BOC Edwards Ltd. and the Engineering and Physical Sciences Research Council. PP gratefully acknowledges the support from the European Union (FP5 Project SICONOS, grant no. IST-201-37172).

References

A. Back, J. Guckenheimer, M.R. Myers, F.J. Wicklin, and P.A Worfolk. DsTool: Computer assisted exploration of dynamical systems. *Notices Amer. Math. Soc*, 39:303–309, 1992.

G.W. Blankenship and A. Kahraman. Steady state forced response of a mechanical oscillator with combined parameter excitation and clearance nonlinearity. *J. Sound Vib.*, 185:743–765, 1995.

C.J. Budd and F. Dux. Chattering and related behaviour in impact oscillators. *Phil. Trans. R. Soc. Lond. A*, 347:365–389, 1994a.

C.J. Budd and F. Dux. Intermittency in impact oscillators close to resonance. *Nonlinearity*, 7: 1191–1224, 1994b.

C.J. Budd, F. Dux, and A. Cliffe. The effect of frequency and clearance variations on single-degree-of freedom impact oscillators. *J. Sound Vib.*, 184:475–502, 1995.

G. Dahlquist and A. Björck. *Numerical Methods*. Prentice-Hall, 1974.

S.L.T. de Souza and I.L. Caldas. Basins of attraction and transient chaos in a gear-rattling model. *J. Appl. Mech.*, 7:849–862, 2001.

S.L.T. de Souza, I.L. Caldas, R.L Viana, and J.M. Balthazar. Sudden changes in chaotic attractors and transient basins in a model for rattling in gear boxes. *Chaos. Sol. Frac.*, 21:763–772, 2004.

S.L.T. de Souza, I.L. Caldas, R.L Viana, A.M. Batista, and T. Kapitaniak. Noise-induced basin hopping in a gearbox model. *Chaos. Sol. Frac.*, 26:1523–1531, 2005.

M. di Bernardo, C.J. Budd, A.R. Champneys, and P. Kowalczyk. *Piecewise-smooth Dynamical Systems: Theory and Applications*. Springer-Verlag, 2007.

J.E. England, B. Krauskopf, and H.M. Osinga. Computing one-dimensional stable manifolds of planar maps without the inverse. *SIAM J. Appl. Dyn. Syst.*, 3:161–190, 2004.

J. Guckenheimer and P. Holmes. *Nonlinear Oscillations, Dynamical Systems, and Bifurcations of Vector Fields*. Springer-Verlag, 1983.

C.K. Halse, R.E. Wilson, M. di Bernardo, and M.E. Homer. Coexisting solutions and bifurcations in mechanical oscillators with backlash. *J. Sound. Vib.*, 305:854–885, 2007.

C.S. Hsu. *Cell-to-Cell Mapping. A Method of Global Analysis for Nonlinear Systems*. Springer-Verlag, 1987.

C.S. Hsu and R.S. Guttalu. An unravelling algorithm for global analysis of dynamical systems: An application of cell-to-cell mappings. *J. Applied Mech.*, 47:940–948, 1980.

B. Krauskopf and H.M. Osinga. Investigating torus bifurcations in the forced van der pol oscillator. In E.J. Doedel and L.S. Tuckerman, editors, *Numerical Methods for Bifurcation Problems and Large-Scale Dynamical Systems*, pages 198–208. Springer-Verlag, 2000.

H. Lamba and C.J. Budd. Scaling of Lyapunov exponents at nonsmooth bifurcations. *Phys. Rev. E*, 50:84–90, 1994.

J.F. Mason, M.E. Homer, and R.E. Wilson. Mathematical models of gear rattle in Roots blower vacuum pumps. *J. Sound Vib.*, 308:431–440, 2007.

S. Theodossiades and S. Natsiavas. Non-linear dynamics of gear-pair systems with periodic stiffness and backlash. *J. Sound Vib.*, 229:287–310, 2000.

P. Thota and H. Dankowicz. On a boundary-value formulation for the continuation of solution trajectories in hybrid dynamical systems and its implementation in the software toolbox TC-HAT. preprint, 2007.